

MICROFLUIDIC TOOLS FOR STUDYING THE SPECIFIC BINDING, ADSORPTION, AND DISPLACEMENT OF PROTEINS AT INTERFACES

Matthew A. Holden¹ and Paul S. Cremer²

¹*Department of Chemistry, Oxford University, Oxford OX1 3QR, United Kingdom;
email: matthew.holden@chemistry.oxford.ac.uk*

²*Department of Chemistry, Texas A&M University, College Station, TX 77843;
email: cremer@mail.chem.tamu.edu (corresponding author)*

Key Words surface chemistry, fibrinogen, Vroman effect, multivalent, ligand-receptor, lipid bilayer, supported membrane, lab-on-a-chip, high throughput, fluorescence microscopy, sum frequency generation (SFG), biofouling, lower critical solution temperature (LCST), polymer folding, and PNIPAM

■ **Abstract** A combination of temperature and concentration gradient microfluidic devices were employed to study the mechanistic details of biomacromolecule interactions at oxide interfaces. These lab-on-a-chip techniques allowed high-throughput, multiplexed data collection using only nanoliters of analyte. The three examples presented demonstrate rapid data acquisition relative to standard methods. First, we show ligand-receptor binding data for multivalent binding between membrane-bound ligands and incoming aqueous proteins with several binding pockets. A model is described for obtaining both the first and second dissociation constant for the reaction. The second example employs temperature gradient microfluidics to study the thermoresponsive properties of polymers and proteins. Both the folding mechanism and subsequent formation of an aqueous two-phase system were followed. Finally, these microfluidic techniques were combined with fluorescence microscopy and nonlinear optical spectroscopy to elucidate the mechanism of fibrinogen displacement from silica surfaces. This combination of methods enabled both direct and indirect observation of protein conformational changes.

1. INTRODUCTION

High-throughput and combinatorial techniques have impacted science in a wide variety of fields (1, 2). For example, organic chemists have exploited spit-pool methods to generate a plethora of pharmaceuticals and other small molecules (3–5). On the other hand, materials scientists have generated thousands of polymers and heterogeneous catalysts by combinatorial screens in search of specific chemical and physical properties (6). Probably the highest impact, however, has been seen in the biological sciences where novel devices from DNA chips (7–10) to multiplexed

capillary arrays are now being used to advance genomics (11, 12), proteomics (13–15), and related systems biology problems. This shift in paradigm of scientific exploration has had far less impact on physical chemistry. This is to be expected, as fundamental studies of matter are not usually compatible with techniques that tackle problems by brute force rather than by obtaining true physical insight. On the other hand, employing new methods for rapid data collection that require only minute sample volumes should open up fields of physical chemistry that are presently inaccessible simply because it takes too long to obtain the required data or the costs and availability of a sufficient amount of sample to perform an investigation are not practical. This is especially true for biophysical studies where proteins, lipids, and sugar molecules may be rare and the required data sets needed to obtain meaningful mechanistic information can be large.

Recently, our laboratory has attempted to fabricate and employ a new generation of microfluidic and lab-on-a-chip-based platforms for obtaining fundamental, molecular level information on topics ranging from protein adsorption (16) and ligand-receptor binding (17, 18), to enzyme catalysis (19–21) and macromolecular folding (22–24). Microfluidic systems possess several properties that make them ideally suited for studying the thermodynamic and kinetic properties of proteins (17, 25–27) as well as enzyme catalysis (4, 20, 28). The small channel dimensions guarantee laminar flow. The mixing behavior of converging streams is therefore easily predicted and the flux through the channels is straightforward to analyze. This is especially convenient, for example, when calculating the turnover rate of enzymes immobilized inside the channels (21, 29, 30). The surface area to volume ratio is much higher in microfluidic systems in comparison to traditional benchtop chemistry and allows for very efficient bulk-surface interaction. The amount of reagent consumed in an experiment is typically no more than a few microliters, making the analysis very cost-effective. Perhaps the greatest advantage of these techniques lies in the tremendous ability to multiplex them (8, 15, 31–34). Many experimental conditions, such as temperature (23, 35–37) and concentration (38–41), can be assayed simultaneously with unprecedented control. This enables rapid data collection with a high signal-to-noise ratio. Furthermore, rapid prototyping (42), which involves curing a polymeric mold against a photoresist master, has made microfluidic technology readily available in a cheap, disposable and easy to reproduce format.

This review presents a survey of recent biophysical experiments. The underlying theme presented here is the derivation of mechanistic information from lab-on-a-chip platforms. The approach here involves the design of fluidic devices specifically tailored for each study. The ability to turn microfluidic designs into physical data from which mechanistic information can be derived rests strongly on array-based architectures.

The review is arranged as follows: In Section 2, we describe three experiments that exploit lab-on-a-chip platforms. First, we discuss a high-throughput method for determining ligand-receptor binding between multivalent proteins and model biomembranes. Second, we describe an on-chip linear temperature gradient

microfluidic device for probing the folding and lower critical solution temperature of thermoactive polymers and proteins. Third, microfluidic technology is combined with more traditional off-chip microscopy and spectroscopy to unravel the biofouling mechanism of the blood protein, fibrinogen, on an oxide surface. In the last section we outline some of the technical details of the methods we have developed for making these measurements.

2. ON-CHIP INVESTIGATIONS

2.1. Multivalent Ligand-Receptor Binding

Solid supported lipid bilayers (31, 43, 44) possess a unique combination of physical properties, which make them well suited to serve as cell membrane mimics. Chief among these is the two-dimensional fluidity of the individual lipid molecules (45, 46). Such mobility is crucial for studies of cell signaling, pathogen attack, and trafficking of lymphocytes, as well as the inflammatory response (47–50). Mobility is required because all these processes involve multivalent ligand-receptor attachment, which relies on the two-dimensional reorganization of cell surface constituents (17, 51, 52). As such, supported bilayer systems have been used to investigate ligand-receptor interactions over the past two decades (53, 54). One particularly interesting puzzle is to unravel how the great variety of lipids in each leaflet of each membrane affects multivalent binding. To answer such a question it is necessary to have convenient methods available to rapidly investigate many different conditions without requiring much analyte. We devised an on-chip method for monitoring an entire adsorption isotherm in a single experiment inside microfluidic channels (Figure 1, see color insert) (17, 18). This allowed detailed information about individual equilibrium dissociation constants to be obtained for proteins that bind to the interface in a stepwise fashion.

Thermodynamic studies were preformed by monitoring fluorescently labeled antibodies binding to ligand-containing membranes coated on the inside of microfluidic channels. Surface specific binding data were collected by total internal reflection fluorescence microscopy (TIRFM). TIRFM is a powerful tool for probing surface adsorption events because light that undergoes total internal reflection at an interface generates an evanescent field that decays exponentially normal to the surface (55). By placing a PDMS (polydimethylsiloxane)/glass microfluidic chip on a dove prism (separated by index matching fluid), collimated radiation from a laser could be passed through the prism and internally reflected to illuminate only those fluorescently labeled proteins near the glass/water interface.

The intention was to create a system where many conditions could be probed simultaneously while using a minimal amount of protein. To do this, a simple array of independent parallel PDMS/glass microchannels was constructed. Small unilamellar lipid vesicles containing a covalently conjugated ligand, 2,4 dinitrophenyl (DNP) were introduced into the channels. Because the process of plasma bonding rendered the PDMS hydrophilic, the vesicles fused to all surfaces of the

microchannel array to form a continuous lipid bilayer coating. Excess vesicles were removed with phosphate-buffered saline (PBS) buffer and fluorescently labeled anti-DNP antibodies, which specifically bound with the DNP, were injected at predetermined concentrations into each microchannel. Surface-bound antibodies were imaged inside the microchannels using TIRFM, and linescans of the images enabled quantitative intensity values to be obtained (Figure 2*a*). TIRFM captured fluorescence mostly from surface-bound proteins; however, the signal also included intensity from antibodies in the near-surface bulk. It was therefore necessary to perform a separate background experiment using a bilayer that contained no DNP ligands. Figure 2*b* shows a linescan of the signal resulting from the near-surface bulk and nonspecifically adsorbed anti-DNP, which was subtracted from the signal in Figure 2*a* to produce a one-shot binding curve of adsorption

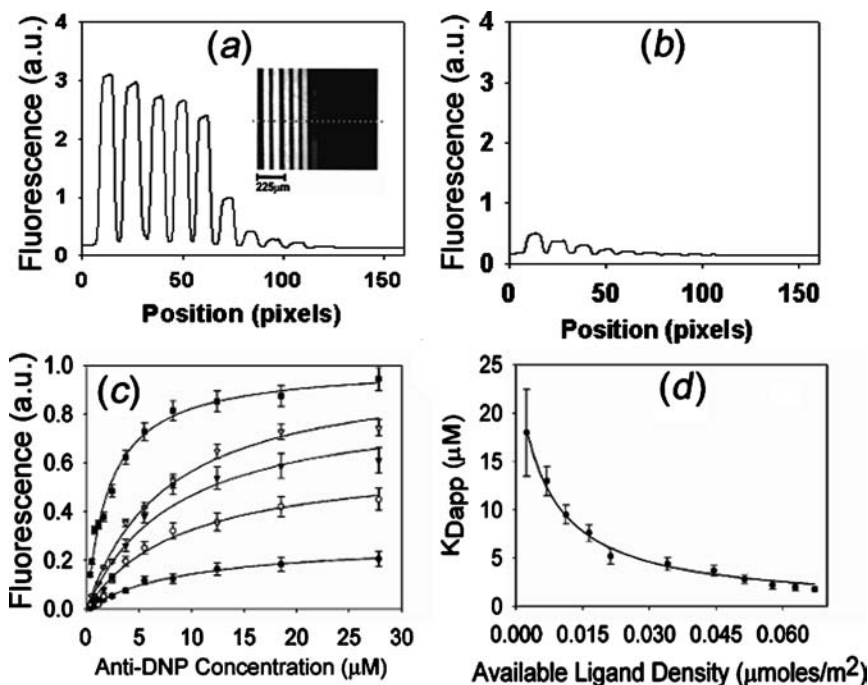


Figure 2 (a) *Inset*: TIRFM (total internal reflection fluorescence microscopy) image of surface-bound Alexa 594 labeled anti-DNP in PDMS (polydimethylsiloxane)/glass microchannels. (a) Fluorescence linescan of the *inset*. (b) Background intensity obtained by arraying protein concentrations from (a) over bilayers, which contained no ligands. (c) Plots of binding isotherms at ligand densities of 0.1 (solid circles), 0.50 (open circles), 0.75 (solid triangles), 1.75 (open triangles), and 3.75 (solid squares) mol% DNP-cap-PE. (d) Plot relating K_{Dapp} with ligand density in solid supported bilayers.

as a function of bulk concentration. Such curves were collected at many different ligand densities and five representative curves are shown in Figure 2c.

The data in Figure 2c could be well fit to simple Langmuir isotherms:

$$\Theta = \frac{K_{App}[B]}{1 + K_{App}[B]}, \quad 1.$$

where the coverage, Θ , depended upon the bulk concentration of the bivalent antibody, $[B]$. Employing this fit yielded the apparent association constant, K_{App} . To interpret the meaning of K_{App} as a function of ligand density in the membrane, the ligand-receptor interaction was modeled as a sequential, two-step binding event. In the first step, the incoming protein binds to the ligand site, L , to form the complex, BL , such that:

$$K_{A1} = \frac{[BL]_s}{[B][L]_s}, \quad 2.$$

where K_{A1} is the first association constant and the subscript, s , on $[L]$ refers to the fact that this is a two-dimensional ligand density, which has units of mol/dm². The second binding event can be represented as:

$$K_{A2} = \frac{[BL_2]_s}{[BL]_s [L]_s}. \quad 3.$$

Moreover, the total number of binding sites on the surface, $[S]_s$, is:

$$[S]_s = [BL_s]_s + [BL]_s/2 + [L]_s/2. \quad 4.$$

From Equations 2–4, the surface coverage can be modeled as:

$$\Theta = \frac{[BL]_s + [BL_2]_s}{2[S]_s} = \frac{\alpha K_{App}[B]}{1 + K_{App}[B]}. \quad 5.$$

This equation has the same form as the Langmuir isotherm in Equation 1, but differs from it in two crucial ways. First, the overall association parameter, K_A , is not a constant, but rather depends on ligand density as: $K_{App} = K_{A1} + K_{A1}K_{A2}[L]_s$. This equation can be rewritten in terms of dissociation constants by replacing each K_{Ai} by $1/K_{Di}$:

$$K_{Dapp} = \frac{K_{D1}K_{D2}}{K_{D2} + 2[L]_s} \quad 6.$$

In this form it can be seen that K_{Dapp} depends on the ligand density as a simple hyperbolic function and that K_{Dapp} becomes equal to K_{D1} as the $[L]_s$ approaches zero.

The second difference between Equations 1 and 5 is the appearance of the parameter, α , which describes the extent of bivalent versus monovalent binding:

$$\alpha = \frac{1 + K_{A2}[L]_s}{1 + 2K_{A2}[L]_s}. \quad 7.$$

The value of α goes to 1.0 when all protein is monovalently bound at the surface (very low ligand densities), but approaches 0.5 when all protein is bivalently bound (high ligand densities). This occurs because bivalent binding competes directly with protein desorption for singly bound species. As ligand density is increased, the protein has a greater chance of achieving bivalent binding.

The use of a high-throughput microfluidic assay is ideal for obtaining binding curves at a sufficient number of ligand densities to obtain K_{D1} and K_{D2} by invoking Equation 6. However, one also needs to take into account the fact that surface-bound ligands are much smaller than an antibody. Indeed, once the ligand density is sufficiently high, the surface can be carpeted with protein without binding all the ligands that are present. Therefore, it is necessary to correct for the available ligand density in Equation 6. This can be done using a simple algorithm (56). Once this is taken into account, the predicted hyperbolic line shape is found for a plot of available ligand density versus K_{Dapp} (Figure 2d). From these data both equilibrium dissociation constants were obtained for the DNP/anti-DNP binding system. The values were $K_{D1} = 24.6 \mu\text{M}$ and $K_{D2} = 0.137 \text{ nmol/dm}^2$. The value for K_{D2} can be used in Equation 7 to obtain information about the extent of multivalent binding as a function of ligand density.

It is possible to use the above equilibrium dissociation constants to obtain free energy values for the first and second binding events by invoking $\Delta G = -RT \ln(K_D)$. This leads to a free energy change of 26.0 kJ/mol for the first binding event and 55.7 kJ/mol for the second. The second value is much greater than the first because of the effective concentration increase in the protein upon going from three dimensions to two. In fact, the standard states of 1 M and 1 mol/dm² used to calculate the free energies are different for these two cases. A three-dimensional equivalent of the second binding constant can be recalculated using Equation 6 if $[L]_s$ is converted to three dimensions by assigning an effective height to the interface. To do this, a value of 10 nm was chosen, which corresponds roughly to the height of the antibody/bilayer thin film. This assumption leads to a free energy change of just 16.1 kJ/mol for the second binding event, which is actually somewhat smaller than the free energy change for the first binding event. Therefore, concentrating the proteins from a three-dimensional box of 1 dm³ to a two-dimensional interface of 1 dm² was equivalent to an effective change in the free energy of ~ 40 kJ/mol.

The value of the assays described above lies in the ability to obtain and compare information about the first and second binding constants as a function of membrane chemistry. Indeed, these techniques should now be useful for making measurements as bilayer constituents like cholesterol, headgroup chemistry, charge on the membrane, sites of unsaturation in the alkyl chains, etc., are altered. The lab-on-a-chip approach makes it possible to obtain a sufficient number of binding curves for obtaining K_{D1} and K_{D2} in a reasonable amount of time with a realistic amount of sample. In Section 2.2, such benefits are taken one step further as both concentration and temperature are altered simultaneously to elucidate mechanisms associated with macromolecular folding and aggregation.

2.2. Temperature Dependent Macromolecular Folding

Although temperature is a fundamental parameter in thermodynamics, it is often overlooked as a controllable variable even in fields of study where high-throughput techniques have otherwise become well established. The reason for this stems from the lack of simple methods for multiplexing temperature the way variables, such as salt concentration or pH, can be conveniently tuned in a 96 well plate format. Nevertheless, it would be especially valuable in molecular level studies to be able to control temperature. We therefore designed a linear temperature gradient microfluidic device to accomplish this goal, with the added benefit of very low sample volume (35). The platform works by placing a heat source and sink in parallel on a chip and arranging a linear array of microfluidic channels inbetween them (Figure 3a, see color insert). Because the temperature must vary linearly from source to sink in this geometry (in accordance with the Fourier heat diffusion equation), the value of the temperature can be read as a simple function of position. This assay is ideal for rapidly obtaining data on the folding of proteins and thermoresponsive polymers.

As a demonstration of the operation of this device, we show the fluorescence yield of semiconductor nanoparticles, the activation energy of a chemical reaction, and the melting curve of a pure substance by collecting all temperature-dependent data simultaneously. In the first example (Figure 3b), the fluorescence quantum yield of CdSe nanoparticles was observed and the *lower inset* shows a 36-channel array from which the data were derived. As expected, the quantum yield decreased as the temperature increased from 13° to 80°C. The *upper inset* gives an idea of the signal-to-noise ratio over a fairly small temperature range (less than 0.1°C between data points). In a second example (Figure 3c), the turnover rate of an alkaline phosphatase enzyme was followed as a function of time at a series of temperatures. A nonfluorescent substrate was flowed over the catalyst, which was immobilized to the microchannel walls. Upon conversion to product, the substrate molecule becomes fluorescent and the reaction can be easily followed, as shown in the inset. The data are well fit by single exponential curves and the plot of $1/T$ versus $\ln(k)$ allows a one-shot Arrhenius plot to be made to determine the activation energy. In a final example (Figure 3d), melting curves are obtained inside the microfluidic platform for 30-bp-long double-stranded DNA. The experiment was performed with a fluorescent dye that intercalates into the DNA when it is double stranded, but is released when the strands melt (57). This behavior causes a sharp decrease in fluorescence because of the increase of the dielectric constant of its surrounding environment (58). As can be seen from the data, it is straightforward to distinguish the subtle difference among the melting curves for complementary DNA strands, those containing a single CA mismatch, and those containing a single TG mismatch. It is this final principle of high-throughput phase transition measurements that is crucial for the studies of thermoresponsive proteins and polymers described below.

2.2.1. LOWER CRITICAL SOLUTION TEMPERATURES FOR POLYMERS Thermoresponsive polymers undergo a phase transition from an elongated and hydrated state to a dehydrated and folded state as the temperature is raised in aqueous solutions (Figure 4a, see color insert). This inverse phase transition behavior, known as a lower critical solution temperature (LCST) (Figure 4a), makes these macromolecules well suited for mimicking the cold denaturation of proteins. Furthermore, the phenomenon can be exploited in a variety of applications in materials science and catalysis (59–61). Poly(N-isopropylacrylamide) (PNIPAM) undergoes an inverse phase transition during which water molecules desorb from the greasy isopropyl moieties of the pendant groups (62). This leads to intramolecular and intermolecular hydrophobic interactions, which cause the polymer molecules to collapse, form aggregates, and ultimately precipitate out of solution (see Figure 4f for PNIPAM structure). The process is readily visible by eye because well-hydrated polymers at sufficiently low temperature scatter very little light, whereas cloudy solutions are formed spontaneously upon raising the temperature above the LCST (usually between 25° and 35°C).

The temperature gradient platform is ideally suited for rapidly determining inverse phase transition temperatures. To do this, a simple optical microscope equipped for dark field detection can be used (Figure 4b). When the polymer molecules aggregate, they scatter a substantial amount of light that is collected through the dark field condenser. Figure 4c shows a typical measurement for PNIPAM made in this fashion. The *inset* shows a close-up of the region where the light scattering is very low (*dark region*) at temperatures below the LCST, but abruptly switches to high scattering intensity (*blue pseudo color region*) where the temperature is above this value. The line profile across this section of the polymer solution reveals that the phase transition takes place over a few tenths of a degree. In a standard experiment, up to six LCST measurements are made simultaneously by placing the requisite number of rectangular glass capillary tubes in parallel across the hot and cold brass tubes. Each individual measurement requires less than 1 μL of solution.

With the technique for rapid LCST measurement in hand, we wished to turn our attention to the mechanism by which mixtures of slightly different polymers fold and aggregate. To explore this problem, several different mole ratios of PNIPAM (63) to poly(N,N-diethylacrylamide) (PDEAM) (64) were examined to determine the initial LCST in pure water. Figure 4d shows that the initial value was lowest for equal mole ratios of PNIPAM and PDEAM and highest for the pure polymers. These data agree well with the notion that the mixed solutions lead to the formation of aggregates containing both PNIPAM and PDEAM. Such mixed aggregates would, of course, have a lower free energy than the corresponding pure polymer particles on entropic grounds. There was, however, another remarkable difference between the behavior of the mixed polymer solutions and those of the corresponding pure compounds. Namely, the LCST curve evolved as a function of time (Figure 4e). It was initially sharp, but then began to develop a kink (at ~ 6 min) and after 9 min a distinct, highly reproducible dip formed, which then stopped

changing with time. This was interpreted to mean that the polymer separated into pure PNIPAM and PDEAM particles after initially undergoing aggregation together (Figure 4a). To confirm this conclusion, additional experiments were performed with differential scanning calorimetry. The results verified that the onset of the LCST was lower for the mixed systems. Furthermore, the overall enthalpy of the process increased continuously as the mole fraction of PNIPAM was raised. Such a result is consistent with the conclusion that a pre-equilibrium is reached whereby the polymers initially come out of solution together. At later times, however, these particles segregate into pure aggregates, presumably on enthalpic grounds.

2.2.2. AQUEOUS TWO-PHASE SYSTEMS The next mechanistic study of a phase transition in a thermoresponsive system involved α -elastin, a protein present in a variety of connective tissues. Like PNIPAM, this biomacromolecule has an LCST, but then goes on to form an aqueous two-phase system (ATPS). By contrast, PNIPAM remains as micron-sized particles after precipitation. ATPS formation is often exploited in processes involving protein, lipid, DNA, and cell separations (65–67). ATPSs form when two incompatible molecules in an aqueous solution phase separate by density under gravitational forces (68). Although both phases still consist mostly of water (75–90 wt%), each phase is dominated by a single component. Typical examples include polymer mixtures or polymers and high concentrations of salt. ATPSs can also occur with a single component as well (69). In this case, all the precipitating particles aggregate together to form a single lower phase, whereas the upper phase is almost pure water or buffer (Figure 5a, see color insert). This is the case for α -elastin.

Despite the widespread use of ATPSs for separations, the mechanism of formation is poorly understood. There are two potential pathways for particle aggregation: coalescence and Ostwald ripening (Figures 5b and 5c). Coalescence involves the direct merging together of high surface tension particles to form larger ones. On the other hand, Ostwald ripening becomes important for lower surface tension particles. In this case, individual polymer molecules are transferred from a shrinking particle to a growing particle (Figure 5c). Big particles grow at the expense of smaller ones because the former have a lower radius of curvature (lower surface free energy) and, hence, polymer molecules do not desorb as quickly from them per unit surface area.

In a first set of measurements, α -elastin solutions at various concentrations of protein were placed across a temperature gradient to monitor their LCSTs (Figure 6a, see color insert). A set of light-scattering profiles taken as a function of temperature reveals that the phase transition is not as sharp as it is for PNIPAM (*bottom linescan*). Moreover, the LCST is concentration-dependent with the lowest value occurring at the highest protein concentration. The profiles changed over time (Figure 6b) with the amount of light scattering continually decreasing. This occurred because a completed ATPS scatters very little light. Many curves were obtained as a function of time and the light scattering intensities were then plotted as a function of time and temperature simultaneously in a three-dimensional plot.

Data for the 30 mg/ml sample of α -elastin are shown in Figure 6c. As can be seen, the amount of light that was scattered decreased in an exponential fashion as a function of time at any given temperature. This decrease occurred fastest at the highest temperatures. At sufficiently low temperature, the amount of scattering intensity was quite low even at early times because the temperature was not above the LCST. It should be noted that obtaining the type of data shown in Figure 6c would be far more difficult to do without using an on-chip method. Traditional methods involve ramping the temperature as a function of time and, hence, do not usually allow data to be gathered isothermally. Even if experiments were carried out in a regular test tube at a single temperature, it would be very difficult to track data for scattering particles that are simultaneously sinking to the bottom of the tube. Moreover, the data collection process would be tedious, require large aliquots of sample, and be very time-consuming.

To gain insight into the mechanism of ATPS formation, the light scattering data in Figure 6c were analyzed quantitatively. It is known in the case of a coalescence mechanism that the number of particles, N_t , decreases as a function of time, t , according to the first-order equation

$$N_t = N_0 \exp(-k_1 t), \quad 8.$$

where N_0 is the initial number of particles and k_1 is the rate constant for coalescence. This single exponential equation fit extremely well to the data in Figure 6c and thus allowed the value k to be extracted both as a function of temperature and concentration. Regardless of the concentration, an activation energy of $9.5 + 0.5$ kcal/mol was found using the Arrhenius equation. This first-order kinetic behavior is consistent with a coalescence mechanism where the activation barrier primarily involves the removal of solvent molecules between two merging α -elastin particles.

The introduction of an anionic surfactant can prevent the pathway leading to coalescence. This is because the surfactant lowers the interfacial tension between α -elastin particles, thereby increasing the activation energy needed to fuse two particles together. The alternative precipitation process of Ostwald ripening (70) occurs when large aggregates grow by accepting single polypeptide strands that desorb from smaller particles. It is not believed that this process is strongly affected by the presence of surfactant (71). The equation in terms of particle number,

$$\frac{1}{N_t} - \frac{1}{N_0} = k_2 t, \quad 9.$$

describes a second-order process during which single-strand desorption and uptake occur simultaneously. The solubility, C , of the protein decreases as the radius of a particle increases. This is expressed by the Gibbs Thompson equation

$$C(r) = C_\infty \exp \left[\frac{2\gamma V_m}{rRT} \right], \quad 10.$$

where C_∞ is the solubility of the protein at a planar interface, γ is the surface tension, V_m is the dispersed phase molar volume, r is the droplet radius, R is the

universal gas constant, and T is temperature in Kelvin. As particles shrink, they begin to shrink even faster. Also, particles that grow continue to do so because their radius of curvature keeps decreasing. These forces shift the equilibrium in favor of growing particles at the expense of smaller ones.

ATPS formation experiments were repeated in the presence of varying concentrations of sodium dodecyl sulfate (SDS). Figure 6*d* shows an example where the concentration of SDS was 1.8 mM. As can be seen, the change in scattering intensity as a function of time was substantially different than without surfactant (Figure 6*c*). In fact, the process did not go to completion, but rather leveled off at longer times. This is typical of an Ostwald ripening process, where the system evolves ever more slowly as a function of time once the average particle size reaches a sufficiently large value. Moreover, the data from this figure could not be well fit to a first-order exponential decay, but fit very well to Equation 9. This fitting gave an activation barrier of 32 ± 2 kcal/mol. This value is more than three times higher than that found for coalescence and reflects the greater energy involved in removing single protein strands from one particle and placing them on another as opposed to merely removing water between coalescing particles.

2.3. Protein Displacement: The Vroman Effect

In the next example, we show how on-chip methods can be combined with more traditional data from microscopy and spectroscopy to elucidate a mechanistic pathway. In this case we studied the displacement of fibrinogen from silica surfaces by blood plasma proteins. Protein adsorption at surfaces is of central interest in fields ranging from stain removal and food processing, to designing biosensors and biological implants (72–75). In the case of implants, it is especially important to understand how blood proteins from the clotting cascade will interact with synthetic materials. Clotting involves a series of complex pathways in which numerous soluble proteins play a role. A key step in this process is the polymerization of human plasma fibrinogen (HPF). It is particularly necessary to keep this macromolecule off an implant surface as its deposition could lead to thrombosis. Unfortunately, surface adsorption of HPF is often unavoidable because it is one of the most abundant proteins in the blood stream (76). Curiously, however, previous experiments have shown that despite the fact that HPF adsorbs rapidly on oxide surfaces, it can be subsequently displaced by proteins that are present at much lower concentrations in human blood plasma (Figure 7*a*, see color insert). This evolution of adsorbate species via displacement is called the Vroman effect (77).

The structure of HPF is shown in Figure 7*b*. Two D domains are tethered to a central E domain by triple-stranded α -helical-coiled coils, and two α C domains interact in a pH-dependent fashion with the E domain. As shown in Figure 7*b*, there is a positive charge on the α C domains at pH 7.4, which creates an electrostatic attraction to the E domain. This attraction aids in a binding interaction between these two moieties. At fairly acidic pH values (~ 3.2), the Lys- and Arg-rich α C domain reversibly detaches as the E domain has its acidic side chains protonated (Figure 7*c*) (78).

We investigated the surface behavior of fibrinogen with AFM, TIRFM, and vibrational sum frequency spectroscopy (VSFS) at a variety of pH conditions. Our main goal was to determine how pH-dependent structural changes affected the desorption behavior of HPF from solid surfaces. We hypothesized that the pH-driven rearrangements of the α C domains could play a major role in this process.

In an on-chip design, silica substrates were incubated with fluorescently tagged HPF molecules at pH 8.0. The surface was subsequently rinsed with buffer followed by a dilute solution of human blood plasma. The fluorescence at the surface was monitored by TIRFM, and the displacement behavior of the protein is plotted in Figure 7*d* (*closed circles*). The decay was best fit using a double exponential function,

$$y = a_1e^{-t/\tau_1} + a_2e^{-t/\tau_2}, \tag{11}$$

where t is time, y is fluorescence intensity, a_1 and a_2 are population fractions between 0 and 1 such that $a_1 + a_2 = 1$, and τ_1 and τ_2 are time constants. The quality of the fit to this equation implies that two distinct populations were being displaced on different timescales. A control experiment revealed that no protein was displaced if plasma was not introduced (Figure 7*e*, *triangles*). In a final experiment, HPF was again adsorbed at pH 8.0. This time, however, the surface was rinsed with buffer solution at pH 3.2 before the pH was again returned to 8.0 and plasma introduced. After such pH cycling, the HPF displacement kinetics was markedly changed (Figure 7*e*, *open circles*). The difference between the pH 8.0 and the pH cycled cases are listed in Table 1.

These results show that after pH cycling the amount of rapidly removed material declines sharply; 80% of the material is associated with slow removal after cycling. Furthermore, the value of the second time constant increased by over fourfold.

To gain insight into this process, we used AFM to scan individual HPF molecules before and after pH cycling, as seen in Figure 7*e*. The D and E domains of the molecule were clearly visible in the image as three individual bumps. After pH cycling, the height of the E domain increased by 1 nm with respect to its initial height, whereas the two D domains remained relatively unchanged. The experiment was repeated dozens of times and this result occurred approximately 80% of the time. The rest of the time all the domains remained unchanged. We reasoned that the height increase could be the result of a rearrangement of the α C domains

TABLE 1

	First time constant, τ_1 , and coefficient, a_1	Second time constant, τ_2 , and coefficient, a_2
pH 8.0 sample	5.3 ± 2.3 min 0.72 ± 0.01	196 ± 98 min 0.28 ± 0.01
pH cycled sample	6.7 ± 3.5 min 0.20 ± 0.02	909 ± 372 min 0.80 ± 0.02

from underneath the adsorbed fibrinogen to the top of the E domain (Figure 7f). To test this hypothesis, HPF was again incubated on the silica substrate inside microchannels. Fluorescently tagged antibodies specific to the α C region were introduced into the channels both before and after pH cycling. It was found that there was at least a sixfold increase in specific binding after pH cycling, indicating that the process increased the exposure of the α C domains to solution as predicted.

In combination with the results from the immunoassay, the fact that HPF could be easily displaced before pH cycling, but not afterward, suggested that the protein adsorbed to the silica via its positively charged α C domains. If true, the Arg and Lys residues of the positively charged α C domains would likely be highly oriented at the negatively charged silica surface. To test this, VSFS was employed. VSFS has the unique ability to probe well-aligned molecular vibrations at interfaces (79, 80). First, a vibrational spectrum of the aqueous/silica interface was obtained (Figure 8a). The peaks at 3200 and 3400 cm^{-1} originate from the OH stretching modes of ice-like and water-like coordination structures (80). The negatively charged silica surface is the driving force behind the water alignment. Upon adsorption of fibrinogen the spectrum changed dramatically (Figure 8b), and an additional feature near 3270 cm^{-1} could be clearly observed. To observe this peak without interference from water structure, the pH of the solution was lowered to 5.5, which brings the entire system close to its isoelectric point without dissociating the α C domains from the E domain. This enabled the sharp peak at 3270 cm^{-1} to become clearly visible. It was also possible to alternate the solution between pH 8.0 and 5.5 several times and reversibly recover the respective spectra in Figure 8b and Figure 8c. However, if the pH was lowered to 3.2 (Figure 8d), the pH 5.5 (Figure 8e) and 8.0 (Figure 8f) looked completely different upon cycling back as the amine peak vanished. These experiments confirmed the presence of well-aligned amine residues under conditions where the α C domains faced toward the surface and the displacement kinetics was rapid. The result is again consistent with the model shown in Figure 8f.

It is quite intriguing to consider the mechanism elucidated above in view of fibrinogen's biological function. Large concentrations of HPF normally present in blood plasma might, at first glance, appear dangerous because of their tendency to bind electrostatically to negatively charged surfaces. The vast majority of cell surfaces carry a net negative charge at physiological pH, but it is likely that the ease with which fibrinogen is displaced plays a key role in keeping these internal surfaces from being coated with a protein that is only one step away from clotting. Therefore, the Vroman effect on artificial materials may simply be a consequence of the body's need to keep it from strongly adhering to endothelial surfaces.

3. MICROFLUIDIC SYSTEM DESIGN

3.1. PDMS and Glass Microchips

Master templates for rapid prototyping were generally prepared by photolithography. UV light was exposed through a photomask to render a pattern into a

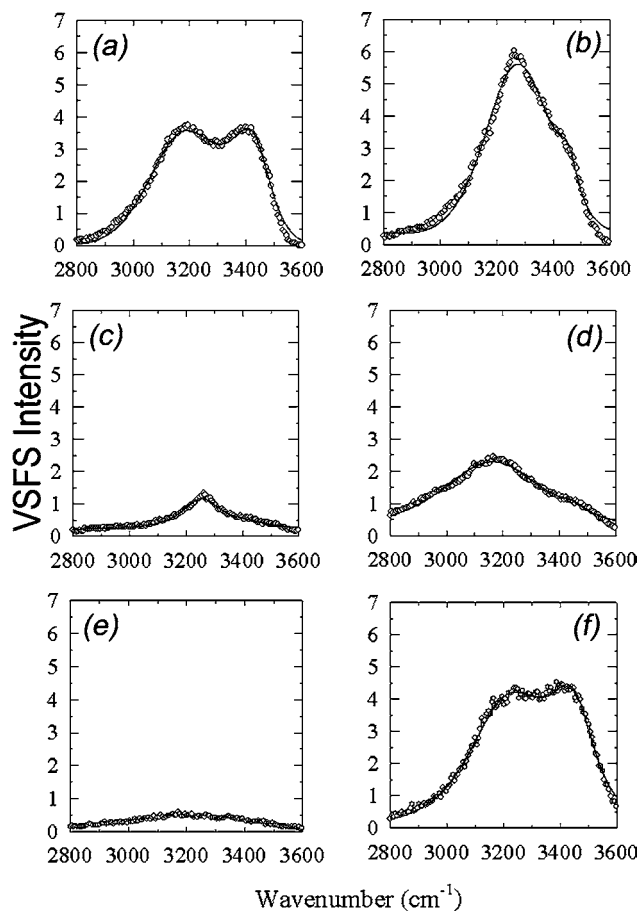


Figure 8 VSFS (vibrational sum frequency spectroscopy) spectra of (a) the silica/water interface at pH 8.0, (b) HPF adsorbed on fused silica at pH 8.0, (c) the same HPF/silica at pH 5.5, (d) pH 3.2, (e) back to pH 5.5, and (f) back to pH 8.0. Note that the sharp feature in (c) cannot be found in (e) after the system is exposed to very acidic conditions.

photoresist coating. Development removed unwanted material, leaving behind a three-dimensional relief over which PDMS could be poured and cured (81). This mold could be covalently bonded to glass or another piece of PDMS by activating the surfaces via an oxygen plasma and then bringing the two into conformal contact. Glass microchips could be prepared by a variety of methods; however, the systems presented in this review were all made using an etching process (82). Photoresist was patterned to reveal the surfaces to be etched. After etching, holes were drilled to allow fluid introduction and finished chips were thermally bonded. More detailed procedures may be found elsewhere (38).

3.2. Solid Supported Lipid Bilayers

Combining solid supported lipid bilayers with microfluidics is a major step toward creating functional biological sensors (17, 18), as microchannel walls can be coated with bilayers containing various ligands or fluorophores. This is achieved by injecting small unilamellar vesicles into the channels, which then fuse to the surfaces. A relatively homogeneous population of vesicles can be produced by either extrusion through nanometer-scale pores or by sonication with a probe tip. Figure 1*a* shows an example of PDMS/glass microchannels coated with lipid bilayers having alternating fluorophore content. Protein solutions were injected, and binding kinetics and thermodynamics characterized. Fluorophore-labeled proteins were visualized by epifluorescence as well as total internal reflection methods, but unlabeled species could just as easily be used and detected by surface plasmon resonance (SPR) spectroscopy, quartz crystal microbalance (QCM) methods, or via electrochemical response.

3.3. Concentration Gradient Microfluidics

Jacobson et al. first demonstrated a device for generating concentration gradients on-chip by developing electrokinetically driven systems which could dilute concentrated analyte streams in series or in parallel (40). Jeon et al. and Dertinger et al. combined pressure-driven flow with a branched microfluidic network to create linear solution and surface gradients (39, 41). Rather than crossing or splitting streams to create gradients, we employed a concept similar to the T sensor, originally pioneered by Yager and coworkers (83–85). Figure 9*a* (see color insert) illustrates the microfluidic diffusion diluter (μ DD) (38). In this example, two dye-containing streams are driven by pressure to a Y junction, where they meet but do not intermix turbulently. Instead, the two streams flow side by side, exchanging contents exclusively by diffusion. At the end of the main channel, a series of parallel microchannels penetrate incrementally deeper into the flowing stream to isolate local concentrations. The shape of the gradient is controlled by flow rate, such that slower flow leads to broader analyte distribution. Figure 9*b* shows a fluorescence image obtained when the flow was 100 nL/min in each inlet, whereas Figure 9*c* shows the fluorescence intensity of both dyes in each microchannel. The slightly asymmetric and nonlinear nature of the gradient can be exploited to create a gradient of analyte that varies over many orders of magnitude between the first and last channel.

3.4. Temperature Gradient Microfluidics

We and others (37, 86, 87) have developed platforms for the creation of linear on-chip temperature gradients. As heat, q , flows between a parallel heat source and cold sink separated by a few millimeters, a linear temperature gradient is established. Figure 3*a* illustrates this concept. The square metal tubes transfer (or abstract) heat to the chip. The cold fluid flow creates a heat sink, whereas either

hot fluid or a thermal electric cartridge creates a heat source. The microchannels can be oriented in parallel with the gradient to establish different temperatures in each channel. Alternatively, the microchannels can be orthogonal to the gradient to create an N versus temperature gradient array, where N is a solution variable (i.e., concentration, composition, etc.). Unlike macroscopic systems, fluid flow in microchannels is subject to rapid temperature changes, some as fast as 10^7 degrees $^{\circ}\text{C}/\text{sec}$ (88). Therefore, the temperature gradient is ideally suited for use in flowing microfluidic channels.

3.5. Multidimensional On-Chip Assay

We combined the μDD with the temperature gradient platform to create an N by temperature array. In this case, the variable N was the concentration of fluorescein dye, which was arrayed in microchannels oriented orthogonal to the temperature gradient as in Figure 9*d*. Aqueous fluorescein concentration ranged from 0 to 266 nM and the temperature ranged from 28° to 74°C . The data collected are plotted in Figure 9*e*. As expected, the highest level of fluorescence intensity occurred at the highest concentration of dye and the lowest temperature. The complex variation over the conditions tested was easily gathered in a single experiment.

3.6. Light-Activated Patterning

Bleached fluorophores were found to rapidly attach to electron-rich surfaces, thereby creating a new visible light patterning method (21, 89), shown schematically in Figure 10*a* (see color insert). Glass substrates were coated with bovine serum albumin (BSA), and fluorophore-tagged molecules were introduced. Depending on the number of labels per molecule, it was possible to create either monolayers or multilayers of patterned species. For example, antibodies that had 3 to 4 Alexa 594 fluorophores per molecule were exposed to intense green light. A general crosslinking occurred such that the aqueous proteins became attached to the adsorbed protein layer and to each other, creating a multilayer. Because not all labels were bleached, the remaining fluorophores of the partially bleached macromolecules were still visible. However, in the case of a ligand-linked fluorophore, only a single label existed per patterned molecule and therefore was no longer visible after patterning. For example, biotin-4-fluorescein was exposed to intense blue light to link the biotin moiety to a BSA-coated surface. Inspection with fluorescence microscopy revealed that no fluorescein could be detected; however, when Alexa 488-labeled streptavidin was introduced, a pattern emerged where the streptavidin bound to the immobilized biotin. Because different fluorophores bleach at different wavelengths, we postulated that two molecules could be patterned from the same solution simply by changing the wavelength of irradiated light. Figure 10*b* shows a fluorescence micrograph of two such species patterned from a single solution. This attachment chemistry took place under aqueous conditions at neutral pH, making it ideally suited for biological assays.

The Annual Review of Physical Chemistry is online at
<http://physchem.annualreviews.org>

LITERATURE CITED

1. Houghten RA, Pinilla C, Blondelle SE, Appel JR, Dooley CT, Cuervo JH. 1991. *Nature* 354:84–86
2. Korbel GA, Lalic G, Shair MD. 2001. *J. Am. Chem. Soc.* 123:361–62
3. Gordon EM, Gallop MA, Patel DV. 1996. *Acc. Chem. Res.* 29:144–54
4. Janda KD, Lo LC, Lo CHL, Sim MM, Wang R, et al. 1997. *Science* 275:945–48
5. Senkan SM. 1998. *Nature* 394:350–53
6. Dickinson TA, Walt DR, White J, Kauer JS. 1997. *Anal. Chem.* 69:341–18
7. Burns MA, Mastrangelo CH, Sammarco TS, Man FP, Webster JR, et al. 1996. *Proc. Natl. Acad. Sci. USA* 93:5556–61
8. Fodor SPA, Read JL, Pirrung MC, Stryer L, Lu AT, Solas D. 1991. *Science* 251:767–73
9. Kopp MU, de Mello AJ, Manz A. 1998. *Science* 280:1046–48
10. Liu QH, Wang LM, Frutos AG, Condon AE, Corn RM, Smith LM. 2000. *Nature* 403:175–79
11. Collins FS, Patrinos A, Jordan E, Chakravarti A, Gesteland R, Walters L. 1998. *Science* 282:682–89
12. Fodor SPA. 1997. *Science* 278:1551
13. Chen XX, Wu HK, Mao CD, Whitesides GM. 2002. *Anal. Chem.* 74:1772–78
14. MacBeath G, Koehler AN, Schreiber SL. 1999. *J. Am. Chem. Soc.* 121:7967–68
15. MacBeath G, Schreiber SL. 2000. *Science* 289:1760–63
16. Jung SY, Lim SM, Albertorio F, Kim G, Gurau MC, et al. 2003. *J. Am. Chem. Soc.* 125:12782–86
17. Yang TL, Jung SY, Mao HB, Cremer PS. 2001. *Anal. Chem.* 73:165–69
18. Yang TL, Baryshnikova OK, Mao HB, Holden MA, Cremer PS. 2003. *J. Am. Chem. Soc.* 125:4779–84
19. Yamaguchi A, Jin P, Tsuchiyama H, Masuda T, Sun K, et al. 2002. *Anal. Chim. Acta* 468:143–52
20. Mao HB, Yang TL, Cremer PS. 2002. *Anal. Chem.* 74:379–85
21. Holden MA, Jung SY, Cremer PS. 2004. *Anal. Chem.* 76:1838–43
22. Zhang YJ, Mao HB, Cremer PS. 2003. *J. Am. Chem. Soc.* 125:15630–35
23. Mao HB, Li CM, Zhang YJ, Bergbreiter DE, Cremer PS. 2003. *J. Am. Chem. Soc.* 125:2850–51
24. Mao HB, Li CM, Zhang YJ, Furryk S, Cremer PS, Bergbreiter DE. 2004. *Macromolecules* 37:1031–36
25. Delamarche E, Bernard A, Schmid H, Michel B, Biebuyck H. 1997. *Science* 276:779–81
26. Chiem NH, Harrison DJ. 1998. *Electrophoresis* 19:3040–44
27. Chiu DT, Jeon NL, Huang S, Kane RS, Wargo CJ, et al. 2000. *Proc. Natl. Acad. Sci. USA* 97:2408–13
28. Eteshola E, Leckband D. 2001. *Sens. Actuators B* 72:129–33
29. Seong GH, Crooks RM. 2002. *J. Am. Chem. Soc.* 124:13360–61
30. Seong GH, Heo J, Crooks RM. 2003. *Anal. Chem.* 75:3161–67
31. Cremer PS, Yang T. 1999. *J. Am. Chem. Soc.* 121:8130–31
32. Delamarche E, Bernard A, Schmid H, Biebuyck H, Michel B, Biebuyck H. 1998. *J. Am. Chem. Soc.* 120:500–8
33. Hovis JS, Boxer SG. 2001. *Langmuir* 17:3400–5
34. Monahan J, Gewirth AA, Nuzzo RG. 2001. *Anal. Chem.* 73:3193–97
35. Mao HB, Yang TL, Cremer PS. 2002. *J. Am. Chem. Soc.* 124:4432–35
36. Mao HB, Holden MA, You M, Cremer PS. 2002. *Anal. Chem.* 74:5071–75

37. Ross D, Locascio LE. 2002. *Anal. Chem.* 74:2556–64
38. Holden MA, Kumar S, Castellana ET, Beskok A, Cremer PS. 2003. *Sens. Actuators B* 92:199–207
39. Dertinger SK, Chiu DT, Jeon NL, Whitesides GM. 2001. *Anal. Chem.* 73:1240–46
40. Jacobson SC, McKnight TE, Ramsey JM. 1999. *Anal. Chem.* 71:4455–59
41. Jeon NL, Dertinger KW, Chiu DT, Choi IS, Stroock AD, Whitesides GM. 2000. *Langmuir* 16:8311–16
42. Xia Y, Whitesides GM. 1998. *Angew. Chem. Int. Ed.* 37:550–75
43. Groves JT, Boxer SG. 2002. *Acc. Chem. Res.* 35:149–57
44. Sackmann E. 1996. *Science* 271:43–48
45. Cremer PS, Groves JT, Kung LA, Boxer SG. 1999. *Langmuir* 15:3893–96
46. McConnell HM, Watts TH, Weis RM, Brian AA. 1986. *Biochim. Biophys. Acta* 864:95–106
47. Mao HB, Cremer PS, Manson MD. 2003. *Proc. Natl. Acad. Sci. USA* 100:5449–54
48. Heldin C. 1995. *Cell* 80:213–23
49. Lees WJ, Spaltenstein A, Kingerywood JE, Whitesides GM. 1994. *J. Med. Chem.* 37:3419–33
50. Mammen M, Choi SK, Whitesides GM. 1998. *Angew. Chem. Int. Ed.* 37:2755–94
51. Lieto AM, Cush RC, Thompson NL. 2003. *Biophys. J.* 85:3294–302
52. Kiessling LL, Pohl NL. 1996. *Chem. Biol.* 3:71–77
53. Pisarchick ML, Gesty D, Thompson NL. 1992. *Biophys. J.* 63:216–23
54. Kalb E, Engel J, Tamm LK. 1990. *Biochemistry* 29:1607–13
55. Axelrod D, Burghardt TP, Thompson NL. 1984. *Annu. Rev. Biophys. Bioeng.* 13:247–68
56. Hlavacek WS, Posner RG, Perelson AS. 1999. *Biophys. J.* 76:3031–43
57. Pirrung MC. 2002. *Angew. Chem. Int. Ed.* 41:1277–89
58. Frutos AG, Pal S, Quesada M, Lahiri J. 2002. *J. Am. Chem. Soc.* 124:2396–97
59. Ito T, Hioki T, Yamaguchi T, Shinbo T, Nakao S, Kimura S. 2002. *J. Am. Chem. Soc.* 124:7840–46
60. Rao GVR, Balamurugan S, Meyer DE, Chilkoti A, Lopez GP. 2002. *Langmuir* 18:1819–24
61. Schild HG. 1992. *Prog. Polym. Sci.* 17:163–249
62. Taylor LD, Cerankowski LD. 1975. *J. Polym. Sci.: Polym. Chem. Ed.* 13:2551–70
63. Freitag R, Baltes T, Eggert M. 1994. *J. Polym. Sci.: Part A* 32:3019–30
64. von Hippel PH, Schleich T. 1969. *Acc. Chem. Res.* 2:257–65
65. Persson J, Nystrom L, Ageland H, Tjerneld F. 1998. *J. Chromatogr. B* 711:97–109
66. Li M, Zhu ZQ, Rodrigues AE. 2002. *Ind. Eng. Chem. Res.* 41:251–56
67. Hatti-Kaul R. 2000. In *Aqueous Two-Phase Systems—Methods and Protocols*, ed. R Hatti-Kaul, pp. 1–10. Totowa, NJ: Humana
68. Lillie MA, Gosline JM. 2002. *Biopolymers* 64:127–38
69. Johansson HO, Persson J, Tjerneld F. 1999. *Biotechnol. Bioeng.* 66:247–57
70. Hanker JS, Giammara BL. 1988. *Science* 242:885–92
71. Hoang THK, La VB, Deriemaeker L, Finsy R. 2002. *Langmuir* 18:10086–90
72. Doolittle RF. 1984. *Annu. Rev. Biochem.* 53:195–229
73. Holland NB, Qiu Y, Ruegsegger M, Marchant RE. 1998. *Nature* 392:799–801
74. Cacciafesta P, Humphris ADL, Jandt KD, Miles MJ. 2000. *Langmuir* 16:8167–75
75. Nieuwenhuizen W, Mosesson MW, De Maat MPM. 2001. *Fibrinogen*. New York: NY Acad. Sci. 645 pp.
76. Nadarajah A, Lu CF, Chittur KK. 1995. In *Proteins at Interfaces II*, ed. TA Horbett, JL Brash, pp. 112–137. Washington, DC: Am. Chem. Soc.
77. Bamford CH, Cooper SL, Tsuruta T. 1992. *The Vroman Effect: Festschrift in Honour of the 75th Birthday of Dr. Leo Vroman*. Zeist, Netherlands: VSP. 192 pp.

78. Shen YR. 1989. *Nature* 337:519–25
79. Kim G, Gurau M, Kim J, Cremer PS. 2002. *Langmuir* 18:2807–11
80. Richmond GL. 2002. *Chem. Rev.* 102: 2693–724
81. Duffy DC, McDonald JC, Schueller OJA, Whitesides GM. 1998. *Anal. Chem* 70:4974–84
82. Fan ZH, Harrison DJ. 1994. *Anal. Chem.* 66:177–84
83. Weigl BH, Yager P. 1999. *Science* 283: 346–47
84. Hatch A, Kamholz AE, Hawkins KR, Munson MS, Schilling EA, et al. 2001. *Nat. Biotechnol.* 19:461–65
85. Schilling EA, Kamholz AE, Yager P. 2002. *Anal. Chem.* 74:1798–804
86. Buch JS, Kimball C, Rosenberger F, Highsmith WE, DeVoe DL, Lee CS. 2004. *Anal. Chem.* 76:874–81
87. Kataoka DE, Troian SM. 1999. *Nature* 402:794–97
88. Lowe H, Ehrfeld W. 1999. *Electrochim. Acta* 44:3679–89
89. Holden MA, Cremer PS. 2003. *J. Am. Chem. Soc.* 125:8074–75

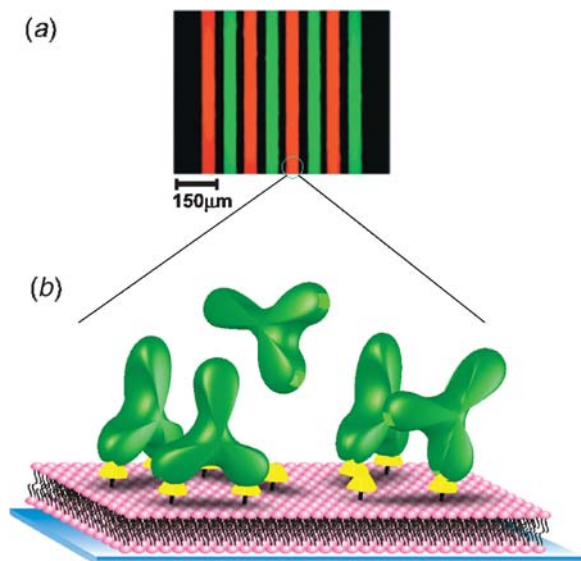


Figure 1 (a) Lipid bilayers fused to the walls of PDMS (polydimethylsiloxane)/glass microchannels. The bilayers contained a small fraction of either Texas Red or fluorescein conjugated lipids for visualization. (b) Antibodies were injected into each microchannel for specifically binding with incorporated ligands. Arrays of channels, each with a unique set of solution or surface conditions, were used to rapidly gather large amounts of data from small sample volumes.

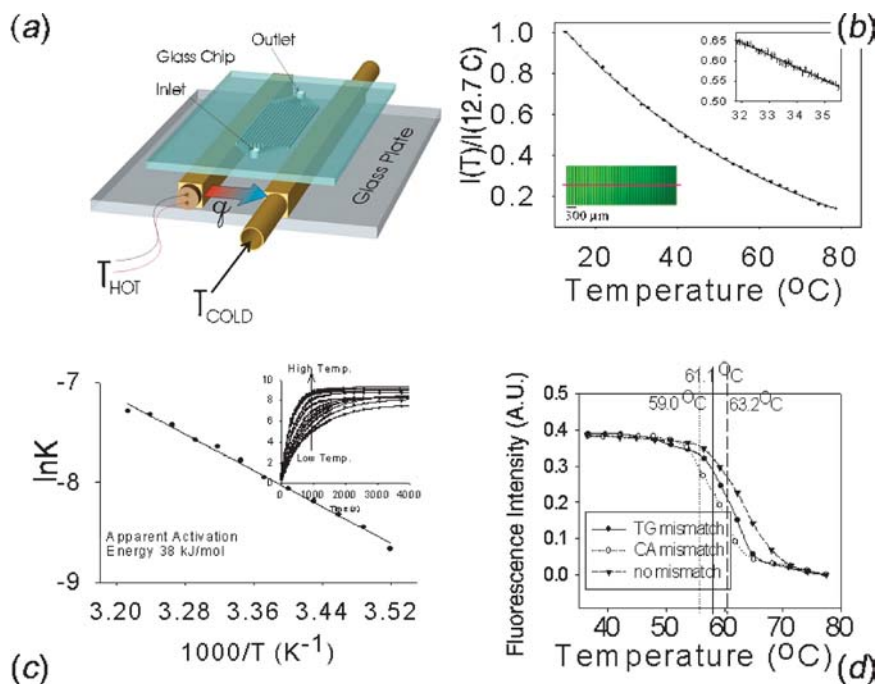


Figure 3 (a) Schematic diagram of a linear temperature gradient platform. (b) CdSe nanocrystals were introduced into microchannels placed inside a linear temperature gradient. The *lower inset* shows the fluorescence image related to the plot in (a). The *upper inset* demonstrates a gradient over a smaller temperature range. (c) The temperature-dependent turnover of substrate by an alkaline phosphatase (*inset*) was observed at many temperatures in a single experiment. Subsequently, we calculated the activation energy using the Arrhenius equation. (d) DNA mismatch melting curves. The shift in melting point was indicative of the type of polymorphism.

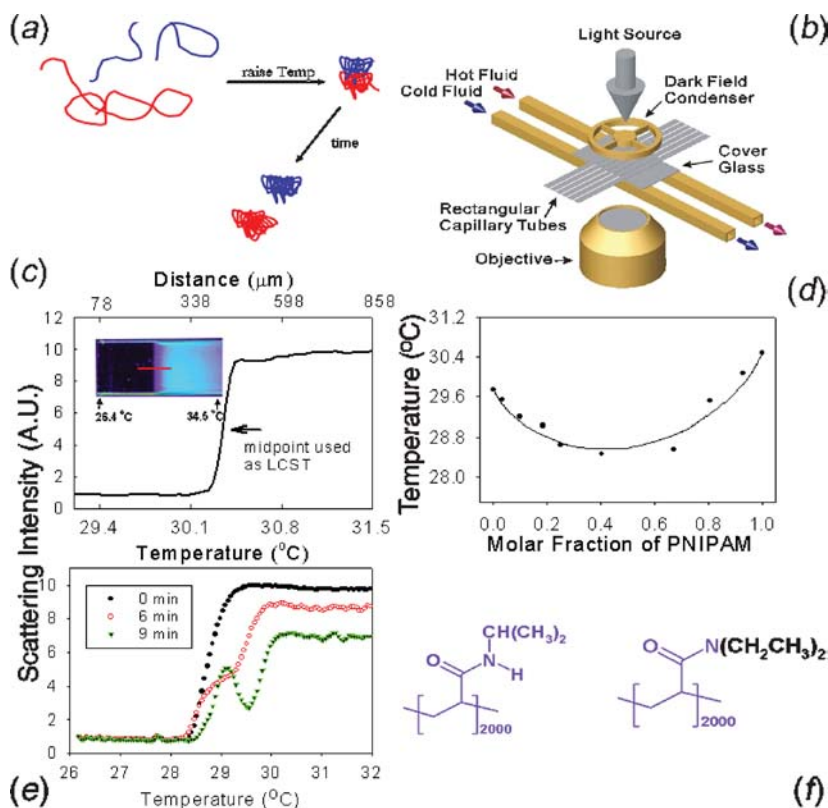


Figure 4 (a) Schematic diagram of a proposed lower critical solution temperature (LCST) mechanism. The polymer chains collapse as a mixed aggregate when water is lost. This is followed by separation of the particles into chemically pure species. (b) Six microfluidic glass capillaries are arranged on a glass coverslip, which spans the temperature gradient. Light scatters from large colloidal particles as polymers exceed the LCST as in (c). (d) Plot of the initial LCST of poly(N,N-diethylacrylamide) (PDEAM) and poly(N-isopropylacrylamide) (PNIPAM) as a function of PNIPAM mol%. (e) Time evolution of a PNIPAM/PDEAM mixture begins with a single sharp LCST, but the system phase segregates later. This was visible as a dip in the LCST curve. (f) Structure of PNIPAM (left) and PDEAM (right).

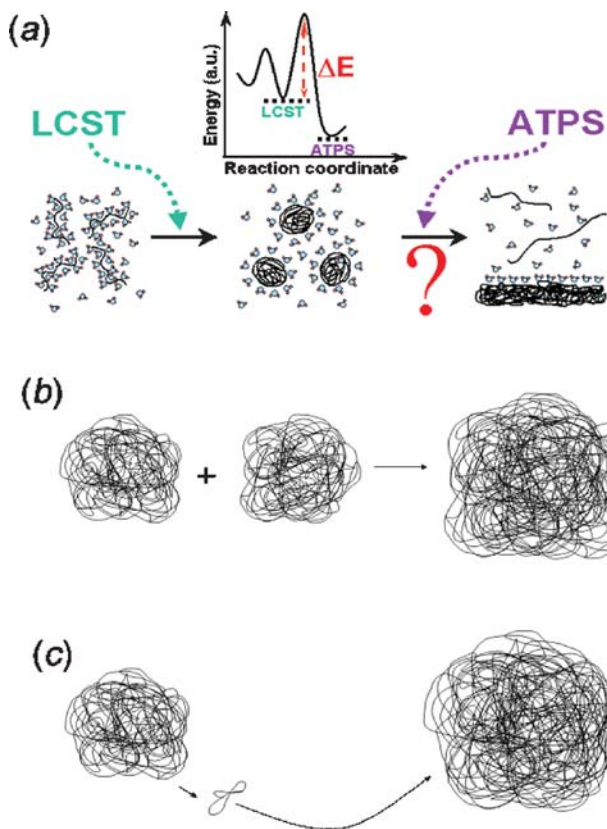


Figure 5 (a) Schematic representation of ATPS (aqueous two-phase system) formation. (b) Coalescence dominates when the surface tension is high. (c) In Ostwald ripening, individual monomers leave the surface of small low-surface-tension particles and adsorb to larger particles.

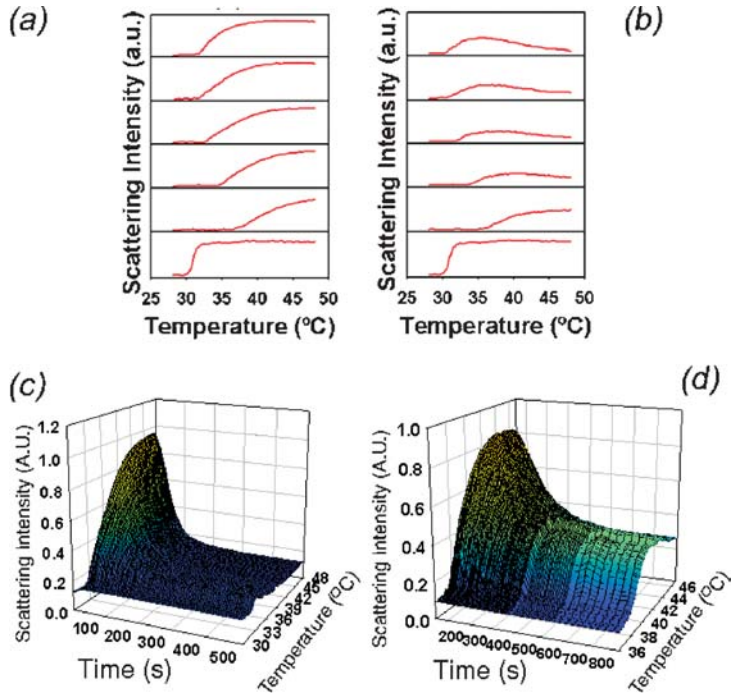


Figure 6 (a) α -elastin lower critical solution temperature (LCST) curves at concentrations of (top to bottom) 40, 34, 30, 24, and 20 mg/ml at $t = 0$ and (b) at $t = 100$ s. Note that the bottom line profile in each is from a 10 mg/ml PNIPAM [poly(N-isopropylacrylamide)] sample that was added as a reference. (c) α -elastin LCST curves taken over time and (d) retaken in the presence of surfactant.

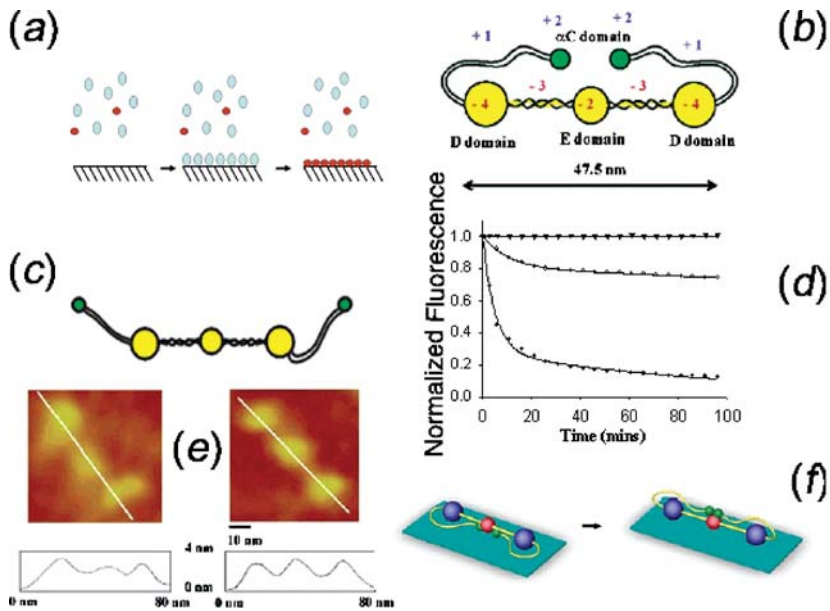


Figure 7 (a) An example of the Vroman effect whereby weakly adsorbed proteins are displaced by more strongly adsorbing species. (b) Structure of fibrinogen. (c) In solution, the α C domains release from the E domain at low pH. (d) Fibrinogen desorption kinetics in the presence of pure buffer (*triangles*), 5% human plasma (*closed circles*), and after (*open circles*) pH cycling. (e) AFM (atomic force microscope) images depicting the height change before (*left*) and after (*right*) pH cycling. (f) Proposed rearrangement model in which the α C domains of fibrinogen are displaced from the substrate by pH cycling. After cycling, the domains rebind atop the central E domain.

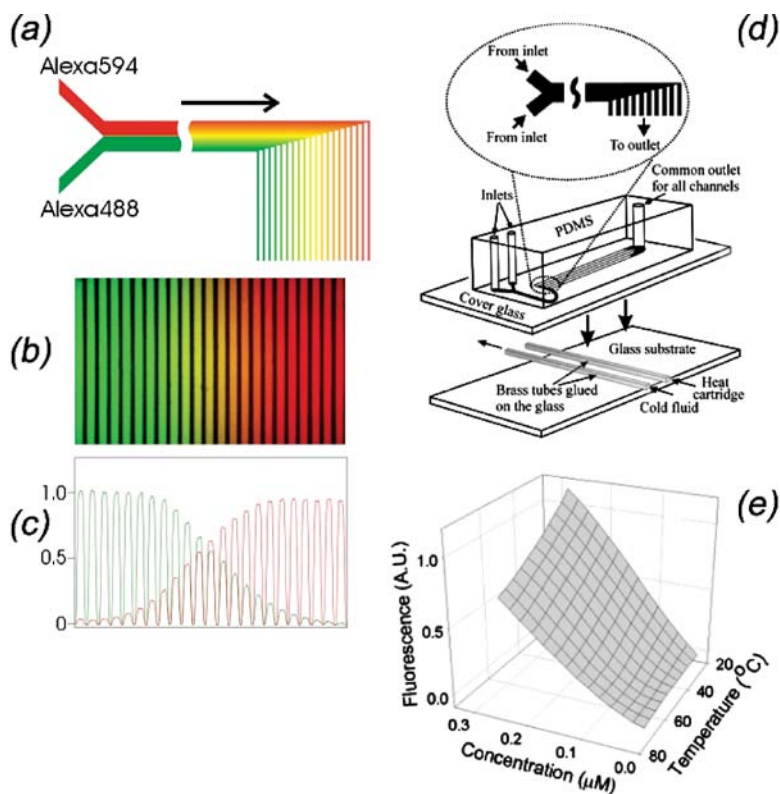


Figure 9 Gradient tools. (a) Schematic diagram of a microfluidic diffusion diluter. (b) Epifluorescence micrograph obtained when red and green dyes were infused into the device at 100 nL/min in each inlet. (c) Fluorescence profile of (b). (d) The microchannels from a concentration gradient were oriented orthogonal to a temperature gradient to create an $N \times$ temperature array, as in (e), where fluorescein fluorescence was observed as a function of concentration and temperature.

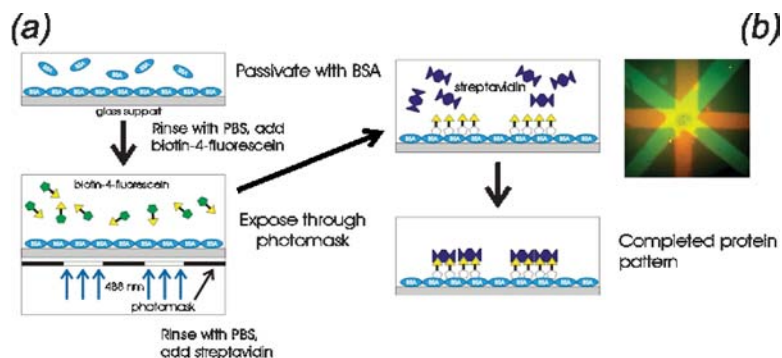


Figure 10 (a) Schematic diagram of a light-activated surface patterning process in aqueous solution. Dye-linked ligand molecules are immobilized on a protein monolayer via photobleaching. Subsequent introduction of a protein, which binds to the ligands, creates a pattern. (b) Dual protein pattern created by immobilizing two dye-linked species from a single solution.

CONTENTS

QUANTUM CHAOS MEETS COHERENT CONTROL, <i>Jiangbin Gong and Paul Brumer</i>	1
FEMTOSECOND LASER PHOTOELECTRON SPECTROSCOPY ON ATOMS AND SMALL MOLECULES: PROTOTYPE STUDIES IN QUANTUM CONTROL, <i>M. Wollenhaupt, V. Engel, and T. Baumert</i>	25
NONSTATISTICAL DYNAMICS IN THERMAL REACTIONS OF POLYATOMIC MOLECULES, <i>Barry K. Carpenter</i>	57
RYDBERG WAVEPACKETS IN MOLECULES: FROM OBSERVATION TO CONTROL, <i>H.H. Fielding</i>	91
ELECTRON INJECTION AT DYE-SENSITIZED SEMICONDUCTOR ELECTRODES, <i>David F. Watson and Gerald J. Meyer</i>	119
QUANTUM MODE-COUPLING THEORY: FORMULATION AND APPLICATIONS TO NORMAL AND SUPERCOOLED QUANTUM LIQUIDS, <i>Eran Rabani and David R. Reichman</i>	157
QUANTUM MECHANICS OF DISSIPATIVE SYSTEMS, <i>YiJing Yan and RuiXue Xu</i>	187
PROBING TRANSIENT MOLECULAR STRUCTURES IN PHOTOCHEMICAL PROCESSES USING LASER-INITIATED TIME-RESOLVED X-RAY ABSORPTION SPECTROSCOPY, <i>Lin X. Chen</i>	221
SEMICLASSICAL INITIAL VALUE TREATMENTS OF ATOMS AND MOLECULES, <i>Kenneth G. Kay</i>	255
VIBRATIONAL AUTOIONIZATION IN POLYATOMIC MOLECULES, <i>S.T. Pratt</i>	281
DETECTING MICRODOMAINS IN INTACT CELL MEMBRANES, <i>B. Christoffer Lagerholm, Gabriel E. Weinreb, Ken Jacobson, and Nancy L. Thompson</i>	309
ULTRAFAST CHEMISTRY: USING TIME-RESOLVED VIBRATIONAL SPECTROSCOPY FOR INTERROGATION OF STRUCTURAL DYNAMICS, <i>Erik T.J. Nibbering, Henk Fidder, and Ehud Pines</i>	337
MICROFLUIDIC TOOLS FOR STUDYING THE SPECIFIC BINDING, ADSORPTION, AND DISPLACEMENT OF PROTEINS AT INTERFACES, <i>Matthew A. Holden and Paul S. Cremer</i>	369

AB INITIO QUANTUM CHEMICAL AND MIXED QUANTUM MECHANICS/MOLECULAR MECHANICS (QM/MM) METHODS FOR STUDYING ENZYMATIC CATALYSIS, <i>Richard A. Friesner and Victor Guallar</i>	389
FOURIER TRANSFORM INFRARED VIBRATIONAL SPECTROSCOPIC IMAGING: INTEGRATING MICROSCOPY AND MOLECULAR RECOGNITION, <i>Ira W. Levin and Rohit Bhargava</i>	429
TRANSPORT SPECTROSCOPY OF CHEMICAL NANOSTRUCTURES: THE CASE OF METALLIC SINGLE-WALLED CARBON NANOTUBES, <i>Wenjie Liang, Marc Bockrath, and Hongkun Park</i>	475
ULTRAFAST ELECTRON TRANSFER AT THE MOLECULE-SEMICONDUCTOR NANOPARTICLE INTERFACE, <i>Neil A. Anderson and Tianquan Lian</i>	491
HEAT CAPACITY IN PROTEINS, <i>Ninad V. Prabhu and Kim A. Sharp</i>	521
METAL TO INSULATOR TRANSITIONS IN CLUSTERS, <i>Bernd von Issendorff and Ori Cheshnovsky</i>	549
TIME-RESOLVED SPECTROSCOPY OF ORGANIC DENDRIMERS AND BRANCHED CHROMOPHORES, <i>T. Goodson III</i>	581
INDEXES	
Subject Index	605
Cumulative Index of Contributing Authors, Volumes 52–56	631
Cumulative Index of Chapter Titles, Volumes 52–56	633
ERRATA	
An online log of corrections to <i>Annual Review of Physical Chemistry</i> chapters may be found at http://physchem.annualreviews.org/errata.shtml	